The Astrophysical Journal, 905:115 (12pp), 2020 December 20 https://doi.org/10.3847/1538-4357/abc3bd

Transition Region Contribution to AIA Observations in the Context of Coronal Heating

S. J. Schonfeld[1] and J. A. Klimchuk[2]
[1] Institute for Scientific Research, Boston College, Newton, MA 02459, USA
[2] NASA Goddard Space Flight Center, Heliophysics Science Division, Greenbelt, MD 20771, USA; schonfsj@gmail.com
Received 2020 August 20; revised 2020 October 13; accepted 2020 October 20; published 2020 December 18

Abstract

We investigate the ratio of coronal and transition region intensity in coronal loops observed by the Atmospheric Imaging Assembly (AIA) on the Solar Dynamics Observatory (SDO). Using Enthalpy-based Thermal Evolution of Loops (EBTEL) hydrodynamic simulations, we model loops with multiple lengths and energy fluxes heated randomly by events drawn from power-law distributions with different slopes and minimum delays between events to investigate how each of these parameters influences observable loop properties. We generate AIA intensities from the corona and transition region for each realization. The variations within and between models generated with these different parameters illustrate the sensitivity of narrowband imaging to the details of coronal heating. We then analyze the transition region and coronal emission from a number of observed active regions and find broad agreement with the trends in the models. In both models and observations, the transition region brightness is significant, often greater than the coronal brightness in all six "coronal" AIA channels. We also identify an inverse relationship, consistent with heating theories, between the slope of the differential emission measure (DEM) coolward of the peak temperature and the observed ratio of coronal to transition region intensity. These results highlight the use of narrowband observations and the importance of properly considering the transition region in investigations of coronal heating.

Unified Astronomy Thesaurus concepts: Solar extreme ultraviolet emission (1493); Solar coronal loops (1485); Solar transition region (1532); Solar electromagnetic emission (1490); Solar observatories (1513); Astronomical models (86); Astronomy data modeling (1859); Observational astronomy (1145)

1. Introduction

A consensus understanding of how exactly the plasma of the Sun's corona is heated to MK temperatures has remained elusive for decades (for more details see reviews by Zirker 1993; Walsh & Ireland 2003; Klimchuk 2006, 2015; Parnell & De Moortel 2012; Viall et al. 2020). Many physical mechanisms have been proposed to cause this heating (for lists of many such mechanisms see Mandrini et al. 2000; Cranmer & Winebarger 2019), but the observations needed to distinguish them are fundamentally challenging. The basic difficulty is that, for all mechanisms, the heating is highly time dependent with a small (generally subresolution) spatial scale perpendicular to the magnetic field. In this context, it is convenient to consider magnetic strands, bundles of magnetic flux with approximately uniform plasma properties over their cross section (Klimchuk 2006). These properties evolve in time in a manner that depends strongly on the details of the heating in the strand. The optically thin nature of coronal plasma emission in the extreme ultraviolet (EUV) and X-ray results in confusion between the many overlapping strands along a line of sight (e.g., Viall & Klimchuk 2011). This makes it impossible to study the dynamics of a single heating event in isolation.

Instead, coronal heating must be studied by determining how the bulk, optically thin plasma responds to heating on observable scales (Hinode Review Team et al. 2019). By simulating the observable response of plasma to heating on unobservably small scales it is possible to constrain the properties of the heating with available instrumentation. This is commonly done by simulating the evolution of plasma within individual closed magnetic strands (e.g., Barnes et al. 2016a, 2016b) and then generating the emission due to collections of these strands (Cargill 1994; Warren et al. 2002; Cargill & Klimchuk 2004; Patsourakos & Klimchuk 2008; Warren et al. 2010; Bradshaw & Klimchuk 2011; Reep et al. 2013; Viall & Klimchuk 2013; Lionello et al. 2016; Marsh et al. 2018) in observable instrument channels.

These coronal models must necessarily consider the coupled system with the transition region that moderates the connection between the hot, tenuous corona and the cool, dense chromosphere. In observational terms, the transition region has commonly been defined based on the temperature regime it occupies, $\sim 10^4$–10^6 K. A more appropriate and physically motivated definition is given by considering models of individual magnetic strands and defining the interface between the corona and transition region to be the location where thermal conduction changes from being a loss term above (causing cooling) to a gain term below (causing heating; Vesecky et al. 1979). This is the approach taken in the Enthalpy-based Thermal Evolution of Loops (EBTEL) model originally defined in Klimchuk et al. (2008). The advantage of this definition is that it more faithfully represents the range of possible states available to coronal loop transition regions. In particular, this acknowledges that in hot loops, temperatures commonly associated with the corona (above 10^6 K) can occur in the transition region close to the loop footpoints where the density and temperature gradients are large. It also allows for the transition region of an individual loop to evolve dynamically in time in response to the heating and cooling of the loop as a whole (Johnston et al. 2017a, 2017b, 2019).

Despite being a small fraction of the volume of a loop (both because it is confined to near the footpoints and because the cross-sectional area of a loop typically increases substantially between the high-β photosphere and the low-β corona, e.g., Guarrasi et al. 2014) the higher densities in the transition region mean that it emits brightly in the EUV. Therefore, the origin of observed EUV emission from lines that emit in the few MK

range is not a priori clear. This emission could originate from relatively cooler coronal loops or from the transition regions of much hotter loops. This uncertainty is the motivation for the present study, to determine how much coronal and transition region emission is expected from loop models in the various Atmospheric Imaging Assembly (AIA; Lemen et al. 2012) channels and how this compares with observations. In Section 2 we briefly describe the EBTEL model and the results of varying loop and heating parameters on the modeled AIA emission. In Section 3 we develop a simple procedure to estimate the transition region contribution in AIA observations and apply it to a number of active regions. We summarize our findings and comment on the implications of these results in Section 4.

2. EBTEL Hydrodynamic Simulations

Enthalpy-based thermal evolution of loops (EBTEL; Klimchuk et al. 2008; Cargill et al. 2012a, 2012b) models the time evolution of the coronal-averaged temperature, pressure, and density in a single magnetic strand in 0D. It is able to accurately describe subsonic plasma evolution under gentle and impulsive heating and can approximately treat complex phenomena such as saturated heat flux and non-thermal electron beam heating. A significant feature of EBTEL is its speed; it can compute the evolution of a single magnetic strand for one day of physical time in seconds, orders of magnitude faster than comparable 1D models. Despite the simplicity of the model, EBTEL's results are very similar to the spatial average determined along the length of a 1D simulation (Klimchuk et al. 2008; Cargill et al. 2012a, 2012b). In addition to computing the average coronal properties, EBTEL also determines the coronal and transition region differential emission measures (DEMs) at each time step. Here we use the EBTEL++ implementation described in Barnes et al. (2016a) and available online at https://github.com/rice-solar-physics/ebtelPlusPlus.

One of the simplifications necessary in the formulation of EBTEL is an assumed ratio of the radiative losses in the transition region and corona. In the model, this is represented by the semiconstant $c_1 = R_{\rm tr}/R_c$, where $R_{\rm tr}$ and R_c are the total radiative losses from the transition region and corona, respectively. This ratio depends on the fixed length of the strand, the dynamic plasma temperature (which influences the plasma scale height), and the coronal density (n) relative to the static equilibrium density for a loop with the same temperature ($n_{\rm eq}$). At low coronal densities ($n < n_{\rm eq}$) conduction dominates the coronal losses and the relative transition region emission is particularly strong (Barnes et al. 2016a). At high densities ($n > n_{\rm eq}$) coronal losses are dominated by radiation, and therefore the relative emission from the transition region is reduced (Cargill et al. 2012a). Ignoring corrections for gravitational stratification and details of the radiative loss function, which are included in EBTEL, this ratio smoothly varies with density between the limits

$$c_1 = \frac{R_{\rm tr}}{R_c} = \begin{cases} 2 & n \leqslant n_{\rm eq} \\ 0.6 & n \gg n_{\rm eq} \end{cases}, \tag{1}$$

which have been chosen to produce results consistent with HYDrodynamic and RADiative emission (HYDRAD) 1D loop models (Bradshaw & Mason 2003a, 2003b; Bradshaw et al. 2004; Bradshaw & Cargill 2013) for a wide range of coronal heating scenarios. It is important to note that while these prescriptions have a controlling influence on the total transition region and coronal emission, they do not directly impact the intensity of the individual channels investigated in this study. This is due to the nonuniform temperature response of the AIA channels (discussed in Section 2.4), which results in their preferential sensitivity to plasma of particular temperatures. In a given (real or simulated) observation, a particular channel may measure emission from the transition region, corona, or a combination of the two, independent of c_1.

Table 1
EBTEL Model Parameters

Parameter	Symbol	Low Value	High Value
Strand half length (Mm)	L	20	80
Energy flux (erg cm^{-2} s^{-1})	F	5×10^6	2×10^7
Minimum delay (s)	$t_{\rm min}$	100	1000
Power-law slope	α	−2.5	−1.0

Note. Parameters of models changed for the different simulations. The parameters held constant in all runs are given in Table 2.

EBTEL defines two other constants related to the temperature profile of a 1D strand. One relates the average coronal temperature in the strand, $\bar{T}$, to the apex temperature, T_a:

$$c_2 = \frac{\bar{T}}{T_a} = 0.9 \tag{2}$$

and the other the temperature at the top of the transition region, T_0, to the apex temperature:

$$c_3 = \frac{T_0}{T_a} = 0.6. \tag{3}$$

These values were chosen based on hydrostatic 1D models computed with HYDRAD, but they are found to be reasonable representations when subsonic flows are present. Equation (3) is particularly important for the current investigation since we are interested in the distinction between the transition region and corona. This means that the calculated coronal temperature determines the maximum temperature of the transition region, which is assumed to cover all temperatures between T_0 and chromospheric temperatures. We stress that T_0 is a physically motivated temperature that correctly demarcates the region of steep temperature and density gradients at the base of a coronal loop.

2.1. Power-law Distribution of Heating Events

In these simulations we heat the plasma with a combination of a constant background heating (1% of the total energy input) and symmetrical triangular impulsive heating events. Each heating event has a duration of $t_e = 100$ s and a total energy input per unit volume ϵ_e proportional to the delay time to the next event given by

$$\epsilon_e = 0.99\ t_d \left(\frac{F}{L}\right) = 0.5\ Q_{\rm max}\, t_e, \tag{4}$$

where t_d is the random delay until the next event, $Q_{\rm max}$ is the maximum volumetric heating rate during the event, and F and L are the energy flux and strand half length (in centimeters) given in Table 1. The factor of 0.99 accounts for the 1%

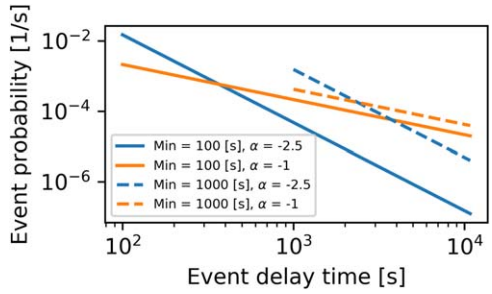

Figure 1. Power-law distributions of heating event delay times. The maximum of each distribution is 10,800 s (3 hr).

constant background heating. The result of this scaling is that each heating cycle has the same time-averaged volumetric heating rate, which is prescribed assuming that the deposited energy is evenly distributed over the length of the loop. The individual heating events are randomly drawn from power-law distributions of heating event delay time (t_d) shown in Figure 1. These power laws are defined by their exponent (α, the slope when visualized in log–log space) and minimum and maximum time delay between events. For all models, the maximum delay time is fixed at three hours (10,800 s), that is, each modeled magnetic strand experiences an impulsive heating event at least once every three hours.

This numerical scheme represents a physical system that is driven with a constant energy buildup rate that releases some fraction of this energy when a critical threshold value is reached. This is consistent with, for example, critical stress reconnection heating driven by random-walk footpoint motion (Parker 1988; López Fuentes & Klimchuk 2015). In this mechanism, the stress in the magnetic field builds with time until a critical level defined in terms of the angle between adjacent magnetic strands is reached, at which point they reconnect and release a fraction of the energy stored in the field. The more energy that is released, the longer it will take for the magnetic field to return to the critical stressed state and reconnect again. Note, however, that the prescribed heating scheme used here does not assume any particular physical mechanism and is consistent with any heating scenario that builds to a threshold level. It also yields similar although not identical (due to the fact that the effects of a heating event are dependent on the physical state of the loop when heating begins) average conditions to systems with constant driving that build to a random stressed state before relaxing impulsively to some constant minimum energy state (Cargill 2014). Similarly, it will emulate any system with a power-law distribution of heating event amplitudes and delay times.

2.2. Modeled Parameters

We perform a parameter space exploration over relevant physical properties of coronal heating. This involves computing EBTEL hydrodynamic models for combinations of four parameters each in two different states for a total of 16 different conditions. These parameters are the length of the magnetic strand, the time-averaged energy flux into the base of the strand (related to the time-averaged volumetric heating rate: $Q = F/L$), the minimum event delay time, and the power-law slope of the distribution of delay times. The parameters explored here represent typical (and by no means extreme) ranges for coronal active regions, where known. These parameters are listed in Table 1 and described below.

2.2.1. Strand Length

We simulate strands with half lengths (footpoint to apex) of 20 and 80 Mm, sizes typical of observable loops in coronal active regions (e.g., those examined in Section 3).

2.2.2. Energy Flux

The total energy losses from the corona in active regions (i.e., the heating necessary for consistency with observations) are $\sim 10^7$ erg cm^{-2} s^{-1} (Withbroe & Noyes 1977) and we heat our models with half and twice this value to simulate weakly and strongly heated regions.

2.2.3. Minimum Delay between Heating Events

"Time lag" analysis of active regions using AIA observations suggests that the characteristic delay between successive heating events is similar to the plasma cooling timescale (Viall & Klimchuk 2017), which depends strongly on the loop length, but is on the order of a thousand seconds. On the other hand, theoretical considerations of reconnection-based heating suggest delays on the order of a hundred seconds (Klimchuk 2015). We therefore test distributions with minimum delay times of 100 and 1000 s.

2.2.4. Power-law Slopes of Event Delays

Many observational studies suggest that flares occur with a power-law distribution (e.g., see discussion in Parnell & De Moortel 2012), and power-law distributions of nanoflares can explain the observed range in DEM slopes coolward of the emission measure peak found in active regions (Cargill 2014). Many theoretical models have also suggested that nanoflares occur with a power-law distribution in energy, from a simple cellular automaton (López Fuentes & Klimchuk 2015) to full three-dimensional magnetohydrodynamic (MHD) simulations (Knizhnik et al. 2018). These models and observational considerations typically find nanoflare energy distributions with power laws of $-2.5 \lesssim \alpha \lesssim -1.5$. However, recent MHD simulations tracking discontinuities in field line tracing by Knizhnik & Reep (2020) suggest nanoflares with time delay and energy power laws with $\alpha \approx -1$. Consequently, our models test heating event power laws with $\alpha = -1$ and $\alpha = -2.5$. Due to the proportionality between the delay time and event energy (Section 2.1), the energy input from the power laws with $\alpha = -2.5$ is small-event dominated while for $\alpha = -1$ it is evenly distributed between events smaller and larger than the average of the smallest and largest events.

2.3. Model Results

Due to EBTEL's speed, we are able to simulate a large amount of solar time in relatively little computational time for this study. Each EBTEL model is run for 10^5 s of solar time and 1000 models with random realizations of impulsive heating are run for each set of parameters to provide a robust average and standard deviation. In total, 1.6×10^9 s of coronal loop evolution are simulated. Those EBTEL parameters that remain constant across all simulations are listed in Table 2.

The evolution of two of these models is shown in Figure 2. For each of these models, the plasma undergoes many heating and cooling cycles in a single run. Some notable (and expected)

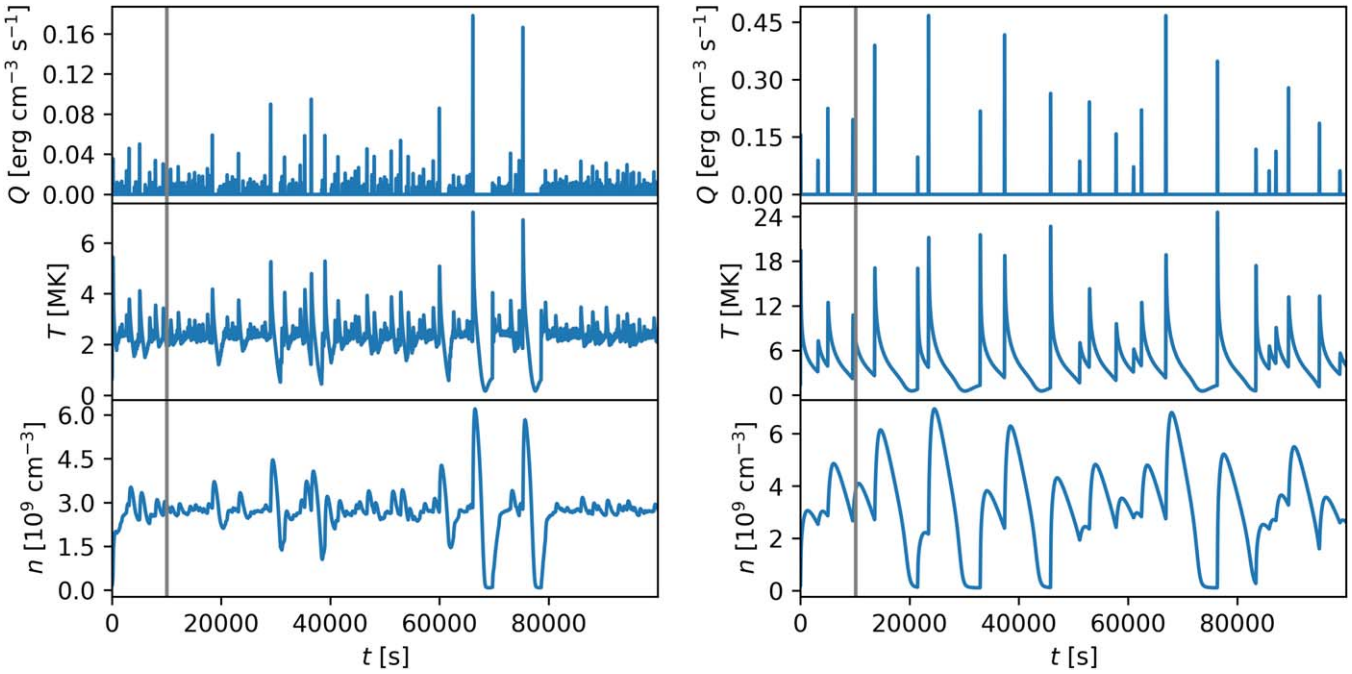

Figure 2. Time evolution of coronal parameters in EBTEL models of individual magnetic strands. Left: a strand with a half length of $L = 20$ Mm, average energy flux of $F = 5 \times 10^6$ erg cm^{-2} s^{-1}, minimum delay between events of $t_{\rm min} = 100$ s, and a power-law distribution of event sizes with a slope of $\alpha = -2.5$. Right: a strand with a half length of $L = 80$ Mm, energy flux of $F = 2 \times 10^7$ erg cm^{-2} s^{-1}, minimum delay between events of $t_{\rm min} = 1000$ s, and a power-law distribution of event sizes with a slope of $\alpha = -1$. The top panels indicate the volumetric heating rate, the middle panels indicate the coronal electron temperature, and the bottom panels indicate the coronal electron density. The gray vertical lines mark the end of the equilibration period after which the runs are averaged.

Table 2
EBTEL Fixed Model Parameters

Keyword *(description)*	Value
total_time *(seconds)*	10^5
tau *(initial time step, seconds)*	1.0
tau_max *(maximum time step, seconds)*	50
force_single_fluid *(electron-ion equilibrium)*	True
use_c1_loss_correction	True
use_c1_grav_correction	True
use_power_law_radiative_losses	True
use_flux_limiting *(for conductive cooling)*	False
use_adaptive_solver *(for dynamic tau)*	True
adaptive_solver_error	1×10^{-6}
adaptive_solver_safety	0.5
c1_cond *(c1 during conductive cooling)*	2.0
c1_rad *(c1 during radiative cooling)*	0.6
helium_to_hydrogen_ratio	0.075
surface_gravity *(relative to solar)*	1.0
dem_use_new_method	True
heating partition *(1 = electron, 0 = ion)*	0.5

Note. Relevant EBTEL parameters held constant for all simulations. More detailed descriptions of these keywords are provided through the EBTEL++ github repository at https://rice-solar-physics.github.io/ebtelPlusPlus/configuration/.

features of these simulations include the typically smaller, more frequent heating events in the model with the shorter minimum delay and steeper distribution of event sizes; the more consistent plasma temperature and density resulting from these more consistent heating events; the more rapid cooling in the shorter strand; and the higher plasma temperatures in the more strongly heated strand with larger heating events.

While the plasma in these models is evolving on individual magnetic strands, the observable signatures of this heating are due to the combination of many hundreds or thousands of such strands evolving within a single resolution element. In addition, because each of these strands is evolving in isolation (due to the extremely high ratio of parallel to perpendicular heat conduction along the magnetic field; van den Oord 1994), the time average of the evolution of a single strand is equivalent to the average of a snapshot of many strands at different phases of their heating and cooling cycles. Because of this equivalence, we not only average all 1000 runs with each set of parameters together, we also average each run over the duration of its evolution, except for the first 10^4 s that are discarded to ensure that the initial conditions of each run have no impact on the results.

The average density and temperature for each set of modeled parameters is given in Figure 3. We can begin to understand the trends by examining the models with the highest frequency of heating events, which most closely resemble steady heating. These are the cases with the shortest minimum delay times ($t_{\rm min} = 100$ s) and steepest distributions ($\alpha = -2.5$). There are well-known scaling laws for loops with truly steady heating, one of which is (Porter & Klimchuk 1995):

$$\bar{T} \propto L^{4/7} Q^{2/7} \propto (LF)^{2/7}, \tag{5}$$

where $Q = F/L$ is the volumetric heating rate. The density of that same loop scales as:

$$n \propto L^{-3/7} F^{4/7} \tag{6}$$

assuming a radiative loss function with power-law slope $\beta = -0.5$ (Rosner et al. 1978). Equations (5) and (6) are often presented with the apex values, T_a and n_a, which have the same scaling but slightly different constants of proportionality. We fit the four high-frequency heating models ($t_{\rm min} = 100$ s and

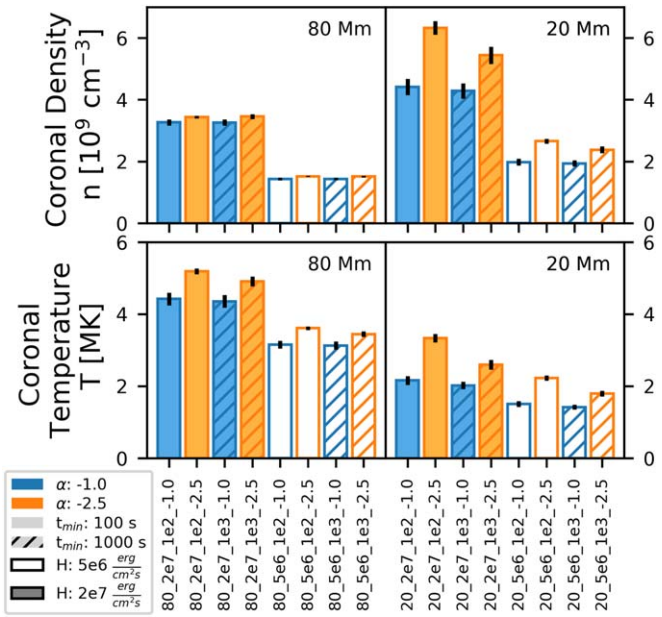

Figure 3. Average coronal plasma density (top) and temperature (bottom) for the 16 tested combinations of the strand parameters. Each simulation is labeled and also indicated by the combination of location (left or right panel), color (blue or orange), pattern (solid or stripped), and shading (filled or empty). The black error lines at the top of each bar indicate the standard deviation as determined by considering the time average of each of the 1000 model runs as a single sample.

$\alpha = -2.5$) with linear regressions between the modeled and theoretical values to determine that the constants of proportionality in Equations (5) and (6) are 0.013 and 0.016, respectively. We then apply these scaling laws to the same models and compare the theoretical average temperatures and densities with the averages determined from the simulations in Table 3. This shows that these EBTEL simulations with the highest frequency heating agree quite well with the equilibrium loop scaling laws. Differences can be attributed in part to differences in the radiative loss function; EBTEL uses a piecewise-continuous β rather than a single value for all temperatures. Models with lower event frequency (longer minimum delay and shallower distributions) have lower average temperatures and densities than the corresponding higher frequency runs. At first this might seem surprising, since high energy events that occur less often produce higher peak temperatures, such as seen in Figure 2. However, the strands cool quickly at these high temperatures and spend the majority of their time in a much cooler state, also characterized by lower density. This dominates the time averages.

2.4. Predicting AIA Intensities

Two of the standard products of the EBTEL simulations are the time dependent DEMs of the corona and transition region. These are the plasma density squared as a function of temperature integrated through their respective portion of the modeled atmosphere. EBTEL assumes the coronal DEM at any given time is narrowly and uniformly distributed around the average coronal temperature in the strand ($\bar{T}$). The transition region DEM is spread between $T_0 = 0.6T_a = 0.67\bar{T}$ and chromospheric temperatures and has a form determined by the energy balance between thermal conduction, radiation, and

Table 3
High-frequency Heating Models Compared with Loop Equilibrium Scaling Laws

L (Mm)	F (erg cm^{-2} s^{-1})	T (MK)	$\bar{T}$ Theory (MK)	n (10^9 cm^{-3})	n Theory (10^9 cm^{-3})
80	2×10^7	5.19 ± 0.08	5.21	3.43 ± 0.04	3.40
80	5×10^6	3.61 ± 0.05	3.45	1.52 ± 0.02	1.45
20	2×10^7	3.33 ± 0.12	3.45	6.32 ± 0.22	6.30
20	5×10^6	2.23 ± 0.07	2.26	2.65 ± 0.08	2.76

Note. Temperature and density scaling of EBTEL models with $t_{\min} = 100$ s and $\alpha = -2.5$ compared with theoretical predictions of steady state equilibrium loops. The EBTEL modeled temperature (T) and density (n) are compared with the theoretical temperature ($\bar{T}$ theory) and density (n theory) determined for the last three models by applying the scaling laws in reference to the first model.

enthalpy. Using the DEMs, we can simulate the expected EUV intensity from each component of the atmosphere. We use the temperature response functions of the "coronal" AIA channels shown in Figure 4 to compute the average coronal and transition region intensities of the simulated strands. These response functions are generated using the IDL routine `aia_get_response.pro` version 8 that utilizes version 7.1.3 of the CHIANTI atomic line database (Dere et al. 1997; Landi et al. 2013).

The emission from a single magnetic strand is of course different from what is observed in a pixel of a high-resolution image. The line-of-sight corresponding to that pixel passes through many different strands of differing lengths. This introduces complexity in interpreting real observations, which we return to in Section 3. For now, we take a simplified approach in order to investigate general behavior. We assume that the emission along a given line of sight can be represented by a single time-averaged strand, i.e., one of our models. A schematic drawing of the basic idea is shown in Figure 1 of Klimchuk & Bradshaw (2014). To facilitate an approximate comparison with observations, we take the line-of-sight depth of the corona to be 40 Mm, comparable to a typical active region scale height, and integrate the coronal DEM from the model over this length to determine the coronal intensities. We then divide this by the transition region intensity from the same model to get a corona-to-transition region intensity ratio, $R_{\rm C/TR}$. The results are shown in Figure 5 for all six "coronal" AIA channels and all 16 models. Note that the models with strand half lengths of 20 Mm and 80 Mm, corresponding to semicircular apex heights of ≈13 and ≈51 Mm, are normalized by the same 40 Mm coronal depth. Differences in coronal brightness between models are not due to differences in depth.

The results from Figure 5 yield the following general trends. In interpreting these trends, it is important to keep two things in mind. First, at any given time during the evolution of a strand, the transition region temperature extends to more than half of the apex (maximum) temperature in the strand (Equation (3)). Second, the classification of heating frequency into high, intermediate, and low is based on the delay between successive heating events relative to the plasma cooling time.

1. In all cases, the ratio is much larger in the 20 Mm strand than the 80 Mm strand. This is due partly to the 40 Mm coronal depth scaling described above. The coronal intensity used in the ratio is over and under represented

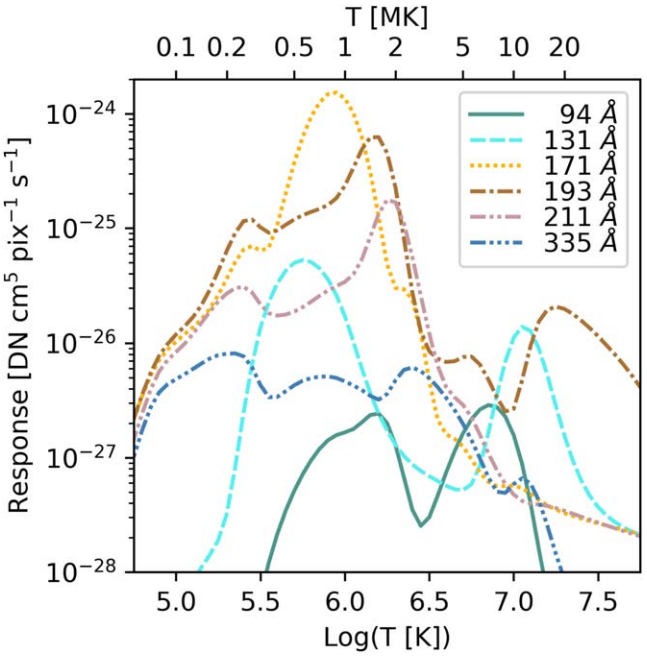

Figure 4. Temperature response functions of the six "coronal" AIA imaging channels. Note that the temperature response of the 171, 193, and 211 Å channels is concentrated near a single temperature (quasi-isothermal), while the 94, 131, and 335 Å channels have a significant response at two or more temperatures.

in the short and long strands, respectively, compared to the full strand length simulated with EBTEL. There is an additional real effect. During a low to intermediate frequency heating and cooling cycle, the transition region emits in a narrow temperature band centered on T for the entire time that the apex is cooling from its peak value to approximately $2T$. The corona, on the other hand, emits at this temperature only for the short time that it takes the coronal plasma to cool through the band. Strands that start their cooling from a higher peak temperature are therefore expected to have a smaller ratio of corona to transition region intensity. Longer strands tend to reach higher temperatures. With strong impulsive heating, the temperature rises to the point at which thermal conduction cooling balances the energy input. This determines the maximum apex temperature. We can estimate this temperature from $Q = F/L \propto T_a^{7/2}/L^2$, which shows that $T_a \propto (FL)^{7/2}$.

2. In the 171, 193, 211, and 335 Å channels, $R_{C/TR}$ is smaller with the larger energy flux, all else equal. This can also be explained by the argument above. Larger F implies hotter T_a, which means that the transition region radiates for longer. The 94 and 131 Å channels often display the opposite effect, which may be due to their second, high-temperature peaks. The 193 Å channel also has a second, high-temperature peak, but its reduced sensitivity compared to the primary peak and its very high temperature mean that it has a negligible influence on the channel response in these modeled loops and solar observations outside of flares.
3. In general, the channels with higher temperature responses (94, 211, and 335 Å) have larger ratios than the channels with cooler temperature responses (131, 171, and 193 Å). A variation of the above argument

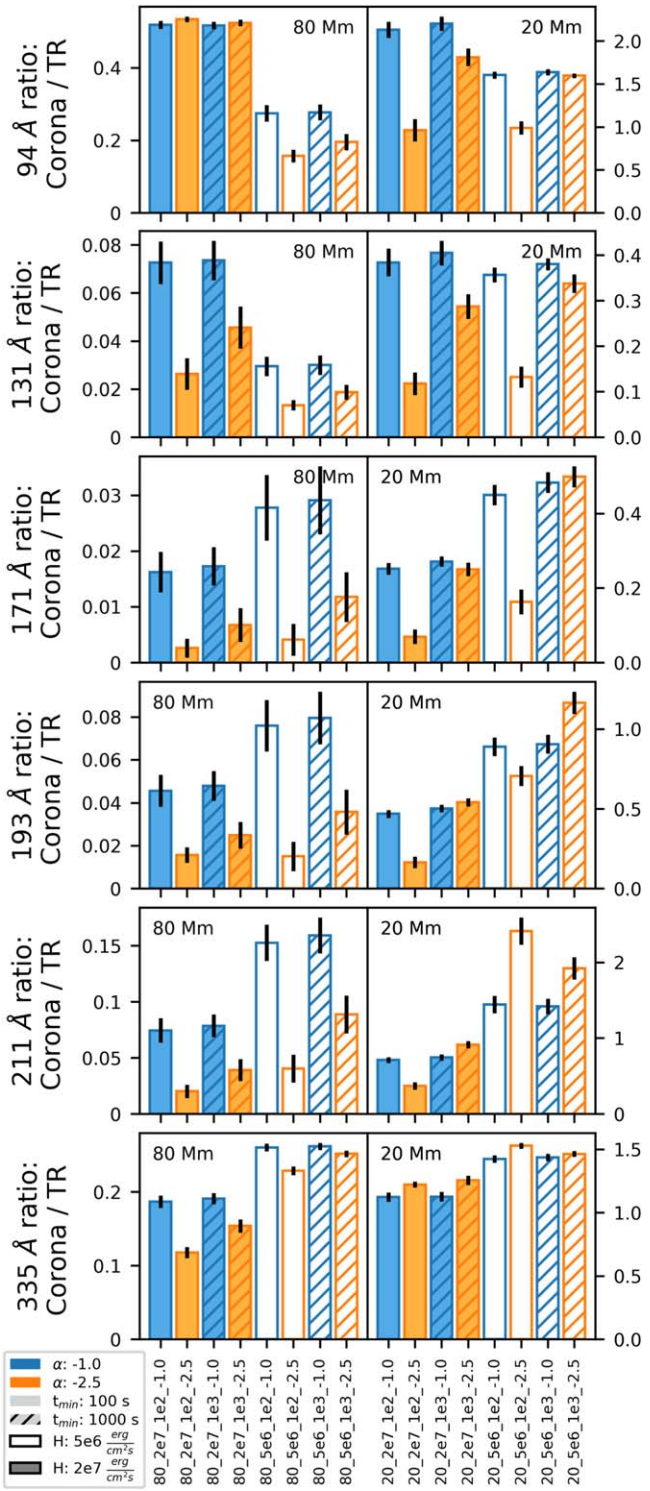

Figure 5. Ratios of coronal to transition region emission in six "coronal" AIA channels for the 16 tested combinations of the strand parameters. Each simulation is labeled and also indicated by the combination of location (left or right panel, with different scales), color (blue or orange), pattern (solid or stripped), and shading (filled or empty). The black error lines at the top of each bar indicate the standard deviation in the ratio as determined by considering the time average of each of the 1000 model runs as a single sample. Note that the ratios for the 20 Mm strands are much larger than the ratios for the 80 Mm strands.

applies here. The maximum apex temperature of a strand is of course the same, regardless of the observing channel. A given T that begins in the transition region at the start of cooling switches to being in the corona

when the apex cools to approximately $2T$. This happens sooner for larger T, so the transition region emission turns off more quickly in hotter channels, and $R_{C/TR}$ is larger. Real channels are of course sensitive to a broad range of temperatures, but the basic concept applies.

4. For cases with $\alpha = -1$, t_{min} has almost no effect. This is because the energy input is dominated by larger heating events with longer delay times.
5. For cases with $\alpha = -2.5$, t_{min} has a large effect, particularly for the 20 Mm strands. This is due to the cooling time of a 20 Mm strand being of order 1000 s, and therefore these small-event-weighted distributions are heated in either a high- or low-frequency regime depending on the choice of minimum cutoff. The effect for the 80 Mm strands is less pronounced since even 1000 s is less than the cooling time.
6. In the 80 Mm strands, the ratios are largest in the low-frequency heating scenarios (with the exception of the 94 Å channel in strands experiencing high energy flux). This is consistent with the findings from Patsourakos & Klimchuk (2008) that found impulsive (nonstatic equilibrium) heating produced larger corona to footpoint ratios in TRACE observations.
7. The arguments above do not apply to models with high-frequency heating, since they experience minimal cooling. Plasma that begins in the corona stays in the corona, and plasma that begins in the transition region stays in the transition region. $R_{C/TR}$ still has a strong temperature sensitivity, but for a different reason. Higher temperature channels are better "tuned" to the corona than to the transition region, so the ratio is larger. A good example is the scenario with $L = 20$ Mm, average energy flux of $F = 5 \times 10^6$ erg cm^{-2} s^{-1}, minimum delay between events of $t_{min} = 100$ s, and $\alpha = -2.5$. The time-series for one of these models is shown in the left panel of Figure 2, which illustrates that the temperature is tightly constrained around the average of 2.2 MK, just above the peak of the 211 Å channel. This set of parameters yields the largest $R_{C/TR}$ in the 211 and 335 Å (which also has significant sensitivity at these temperatures) channels while yielding the lowest $R_{C/TR}$ for models with the same energy flux in the other channels.

Overall, Figure 5 clearly demonstrates that EBTEL models of the solar atmosphere indicate both that the transition region contributes significantly to the intensity of AIA observations and that this contribution has strong dependence on the details of the underlying coronal heating. In the channels with strong response to the lowest temperatures, particularly 131 and 171 Å, this analysis suggests that the majority of observed emission could be due to plasma more accurately attributed to the transition region than the corona, for a wide range of loop lengths. This is also true of the hotter channels in the long loops. Furthermore, in every channel except 335 Å, $R_{C/TR}$ is different by more than a factor of 2 for certain combinations of minimum delay and event distribution power law for a given loop length and energy flux. While these results are difficult to apply directly to the interpretation of observational data, as explained in Section 3, they highlight the importance of considering contributions from the transition region when using observations to characterize coronal heating.

Before proceeding to consider observations, we note that Patsourakos & Klimchuk (2008) used EBTEL simulations to investigate the coronal and transition region emission as observed in the 171 Å channel of the Transition Region And Coronal Explorer (TRACE; Handy et al. 1999). Their approach differs from ours in that they treated observations near the limb, assuming that the line of sight is perpendicular to the plane of the strand, and spreading the transition region emission over 2 Mm vertically from the solar surface. They found intensity ratios of about $1/600$ and $1/35$ for steady and low-frequency impulsive heating, respectively, in a 25 Mm (half length) strand. These ratios correspond to ~0.03 and ~0.6 for our assumed observing geometry (40 Mm coronal path lengths), consistent with what we calculate here. Patsourakos & Klimchuk (2008) emphasized how the larger 171 Å ratios produced by impulsive heating are more in line with observations.

3. AIA Observations

Since the launch of the Solar Dynamics Observatory (Pesnell et al. 2011) in 2010, the AIA (Lemen et al. 2012) has become the default imager for studies of the solar corona. However, as demonstrated in Section 2.4, a significant portion of the light observed in the AIA channels may originate in the transition region rather than the corona. In the following sections, we make simplifying assumptions about the geometry of observed active regions to distinguish the observed coronal and transition region contributions to the six "coronal" AIA channels.

3.1. Observationally Separating the Corona and Transition Region

On the Sun, a single line of sight typically passes through the coronae of one set of strands and the transition regions of an entirely different set of strands, not the corona and transition region of the same strand, as assumed in the modeling described in Section 2. This is only a minor concern for understanding coronal heating if the strands are similar, but that is often not the case. Instead, to compare with the modeled magnetic strands, we must investigate multiple lines of sight containing observed coronal and transition region emissions that are physically linked by the magnetic field. This is possible whenever individual loops, or collections of loops, and their associated footpoint(s) can be identified in an image.

An example for active region NOAA 11268 is shown in Figure 6. We select this region because of its widely separated bipole magnetic field structure with easily identifiable loops that clearly terminate in a compact concentration of strong photospheric magnetic fields. In addition, the loop top region we identify as a sample of the corona (blue box) has very weak photospheric magnetic fields along the line of sight, suggesting that there will be very little contribution from transition region plasma associated with other structures. The smaller orange box identifies the transition region footpoints that we associate with these loops. We analyze the average over five minutes of full cadence (12 s) data in order to minimize the impact of any particularly short-term variability within the region. While this average may incorporate multiple complete heating cycles (e.g., if $t_{min} = 100$s) we expect no information loss from this procedure due to the inherent averaging in the observations caused by the many overlapping and out of phase strands along

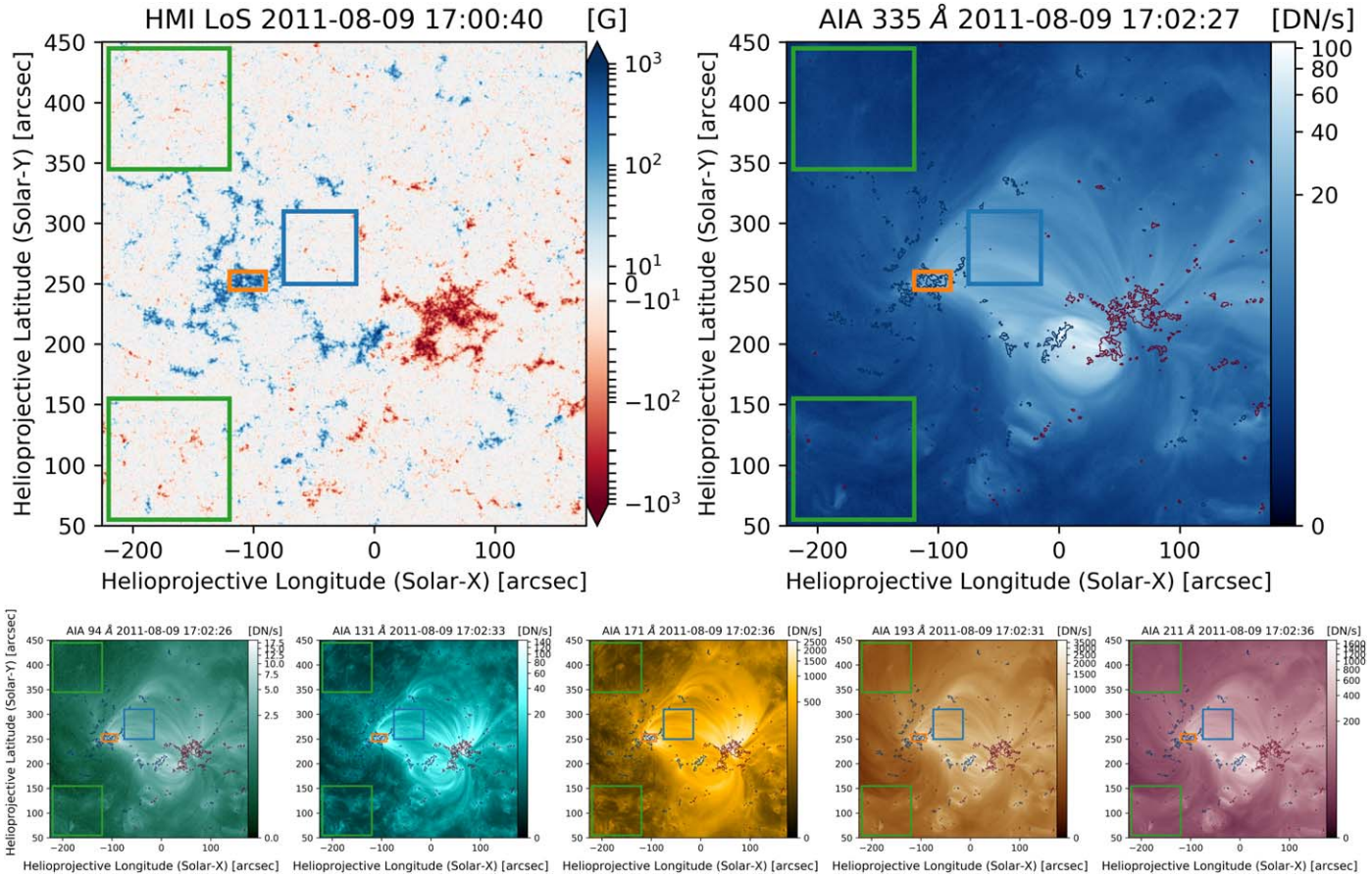

Figure 6. HMI line-of-sight magnetogram and the six "coronal" AIA channel observations of active region NOAA 11268. Each of the AIA images are five minute averages of full cadence data. The green squares indicate the regions designated as quiet Sun, the blue square indicates the loop tops in the corona, and the orange rectangle indicates the footpoints and transition region of these same loops. The blue and red contours in the AIA images indicate the extent of the ±200 G photospheric line-of-sight magnetic field.

a line of sight. This 5 minute averaging is consistent with the procedure from Warren et al. (2012) discussed in Section 3.2.

The average intensities within the boxed regions are used to determine the characteristic coronal and transition region intensities of the prominent loops in this region. Because the photospheric magnetic field within the blue box resembles that within the quiet Sun, we subtract the average intensity of the quiet Sun (identified by the green boxes in the upper and lower left corners) from the intensity of the corona (blue box). This has very little impact on the analysis because the quiet-Sun intensity is small compared to the loop intensity in these channels. We make two different assumptions about the source of the intensity in the orange box that we call the transition region. First, we assume that all of the emission comes from the transition region. Second, we acknowledge that some of the intensity is due to the overlying corona, and assume that the coronal component is identical to that in the blue box. This is likely an overestimate because we expect coronal emission to diminish from the polarity inversion line outward, both horizontally and vertically, because the heating rate varies directly with the magnetic field strength. Shorter strands tend to be brighter—due to their increased density, as seen in Figure 3—and the line of sight intersects more short strands in the blue box than in the orange box. See Figure 1 in Klimchuk & Bradshaw (2014).

The observed $R_{C/TR}$ using both assumptions about the contribution of the corona to the orange box is plotted for each channel in Figure 7. In all cases, the blue bars indicate that the transition region is brighter than the corona. When we take into account that there will be some contribution from the corona in the box identified as the transition region, the ratio increases, and significantly in the case of the 211 and 335 Å channels. This is not surprising since, in this small active region, we might expect these two relatively hotter channels to be the brightest in the corona, as can be seen in the images. In reality, the true ratios likely fall somewhere between the blue and orange bars in Figure 7.

While we do not anticipate any single EBTEL model will agree with the ratios observed in this active region, because it contains contributions from a large number of magnetic strands of differing length and, presumably, heating properties, it is encouraging to see the same general trends as those identified in the models. Regardless of the foreground coronal subtraction, the transition region is brighter than the corona in the 131 and 171 Å channels that are sensitive to lower temperature plasma and the corona is relatively brighter in the 211 and 335 Å channels that are sensitive to hotter plasma. The 193 Å channel samples intermediate temperatures and exhibits an intermediate ratio. The fact that the 94 Å ratio closely resembles that of 171 and 193 Å suggests that its emission is dominated by the low temperature peak in its temperature response function (Figure 4) and therefore that there is less plasma near ∼5 MK than near ∼1 MK.

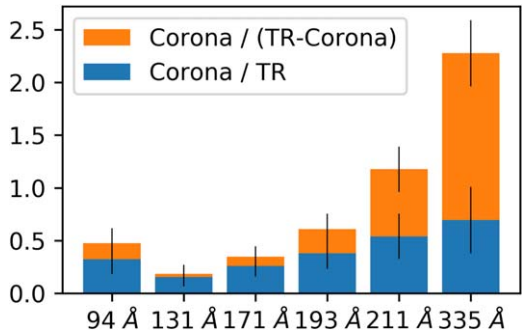

Figure 7. Observed $R_{C/TR}$ in the six "coronal" AIA channels for active region NOAA 11268. The blue bars represent a scenario where there is no overlying corona in the transition region (orange box) while the orange bars assume that the identified coronal intensity (blue box) is also present in the transition region. The true ratios likely fall between these two representations.

3.1.1. The Impact of Loop Geometry

In addition to the single strand/multistrand difference, there are geometrical effects that impact the comparison of the modeled and observed intensity ratios. The observed loops, or at least their envelope, appear to be considerably more compact (particularly in latitude) at their footpoints than at their apexes. Hence, the orange transition region box is smaller than the blue coronal box. The intensities that are used in the ratios are the spatial averages over the boxes. The coronal value is smaller than would be the case if all the emission were confined to a smaller area, i.e., an expanding versus nonexpanding loop. Since the models do not account for this effect, the modeled corona-to-transition region intensity ratios would need to be decreased for a more direct comparison with the observed ratios. Another geometric difference is that the models assume a coronal path length of 40 Mm, whereas the line-of-sight depth of loops within the blue box could be larger or smaller. Finally, the coronal values from the models are the spatial averages along a strand, whereas the observed coronal intensities are near the loop apexes. Gravitational stratification would suggest that the modeled ratios should be decreased somewhat for a more direct comparison with the observations, particularly for the 80 Mm loops.

Since the modeled ratios are, if anything, too small compared to the observations, these corrections would make the discrepancy worse. However, we stress that the modeled ratios are highly idealized. The point of the present study is not to reproduce the observations as closely as possible, but rather to (1) demonstrate that the transition region makes an important contribution to intensities observed in AIA "coronal" channels and (2) demonstrate that $R_{C/TR}$ is sensitive to the details of the heating and therefore has diagnostic potential. In future work, we will construct more realistic models along the lines of those in, e.g., Warren & Winebarger (2006, 2007), Lundquist et al. (2008a, 2008b), Bradshaw & Viall (2016), Nita et al. (2018), and Barnes et al. (2019).

3.2. Analyzing the Warren et al. (2012) Active Regions

For each of the 15 active regions studied in Warren et al. (2012; except their Region 13 Box 2) we repeat the analysis performed in Section 3.1. The regions identified as coronal are those defined and analyzed in the original paper while the transition region boxes are determined by eye based on the apparent connectivity of the loop features in each region. These active regions and the associated boxes indicating the corona, transition region, and quiet Sun are shown in Figure 8. We expect that the wide range of active region structures and viewing geometries represented in this sample will minimize any particular geometrical bias introduced by analyzing a single region. In addition, these regions represent a wide range of physical scales with potentially different heating properties.

We compute $R_{C/TR}$ in each channel for each active region individually. The distributions of these ratios are plotted in Figure 9. Notice that while the ratios are on average larger than the ratios found in NOAA 11268, in most cases the transition region is still brighter than the corona. Only in the 94 and 335 Å channels is this not generally the case. Previous analysis of these active regions determined that they have DEMs peaking between $\log(T\ [\mathrm{K}]) = 6.5$–$6.6$, where the 94 and 335 Å channels have the highest relative response. It is not surprising, therefore, that $R_{C/TR}$ is greatest in these channels. While there is some plasma above the DEM peak, the slopes of the DEMs are quite steep, and there is very little plasma at $\log(T\ [\mathrm{K}]) \sim 7.1$, the temperature of the strong secondary peak in the 131 Å channel. The 131 Å intensity ratios are consequently smaller, although still elevated compared to NOAA 11268.

Warren et al. (2012) measured the power-law index of the DEM distribution in the range $6.0 \leqslant \log(T) \leqslant 6.6$ (approximately the peak temperature) in each of the coronal boxes in Figure 8. This is the slope, α_{DEM}, in a log–log plot. We compare the coronal DEM slopes with $R_{C/TR}$. A sample of these relationships is shown for the 171 and 335 Å channels in Figure 10. There is a clear anticorrelation in the 171 Å channel, in which larger intensity ratios correspond to smaller slopes, i.e., flatter DEM distributions. The same trend appears in the 335 Å channel, but with much larger scatter. To quantify the trends, we perform multiple statistical analyses, as reported in Table 4. Because the distributions appear approximately linear, we compute the Pearson correlation coefficient. The negative coefficients indicate the inverse relationships while the larger magnitudes of the 171, 193, and 211 Å channels indicate tighter correlations (less scatter).

One disadvantage of the Pearson analysis is that it assumes that the measured quantities are normally distributed, i.e., that the errors in the measurements follow a normal distribution. We have no indication that this is or is not the case. We therefore also perform a nonparametric, or rank ordered, statistical analysis, which is valid for any measurement distribution. We use the weighted t-statistic described in Efron & Petrosian (1992), following the implementation in Porter & Klimchuk (1995). The probability that α_{DEM} and $R_{C/TR}$ are random is given by $P(tw)$ in Table 4. A small value indicates a high probability of correlation. The fourth column indicates the most probable χ in the assumed relationship $R_{C/TR} \propto (\alpha_{DEM})^{\chi}$, and the final column gives the 90% confidence interval of χ. From these analyses, we see that all channels except 94 and 335 Å have robust inverse correlations. The relationship between α_{DEM} and $R_{C/TR}$ in the 94 and 335 Å channels is likely random, which could be due to their significantly nonisothermal temperature response functions. Again, the 131 Å channel is functionally isothermal in these observations because there is very little plasma above 10 MK in these regions.

Warren et al. (2012) also measured the slopes of the coronal DEM with $\log(T) \geqslant 6.6$, hotter than the peak. We compare those slopes with the intensity ratios and find no significant correlation in any channel.

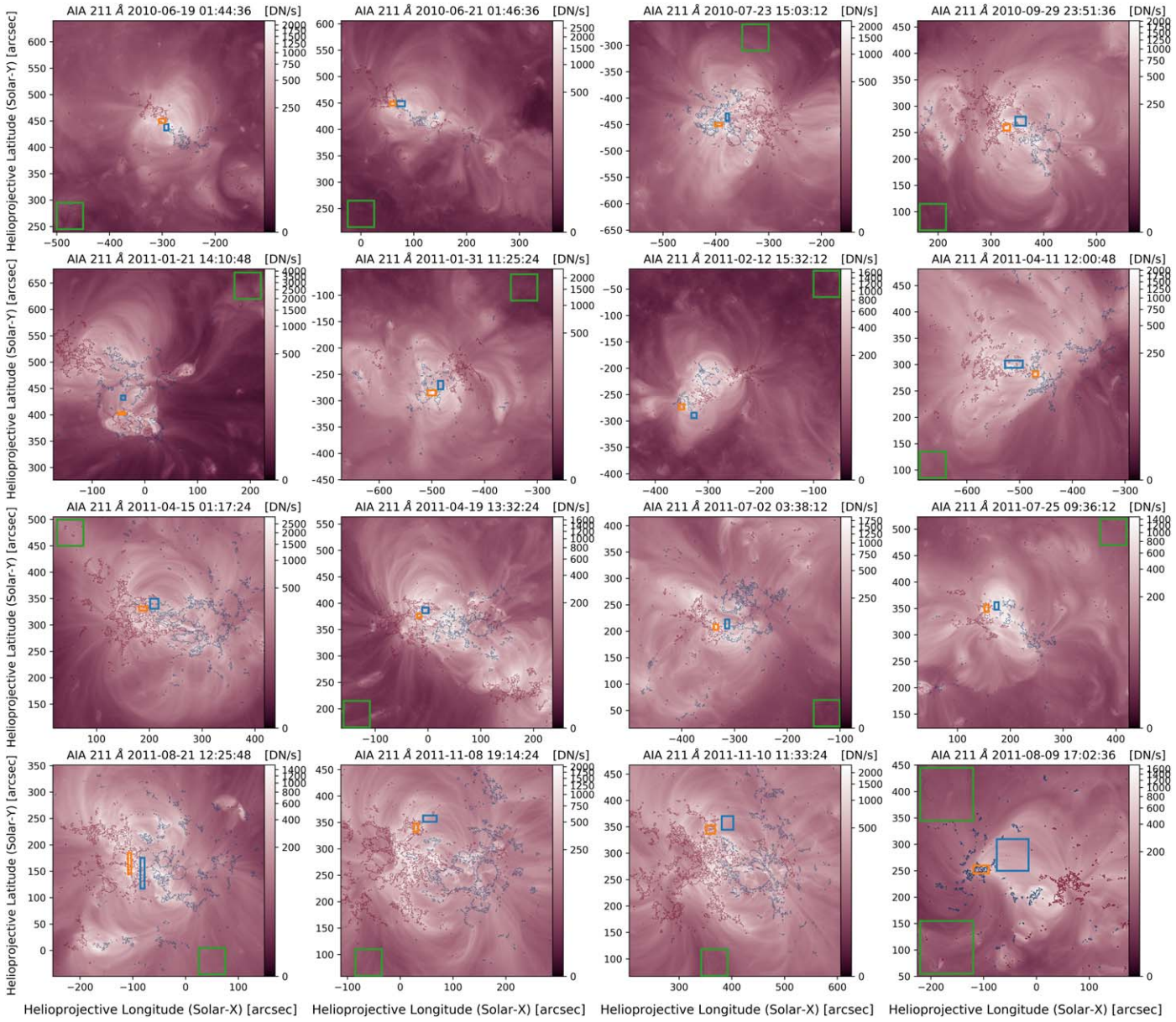

Figure 8. AIA 211 Å five minute average images of the active regions from Warren et al. (2012). The boxed regions and contours highlight the same features as in Figure 6. The bottom right panel shows the individual region from Figure 6 for comparison.

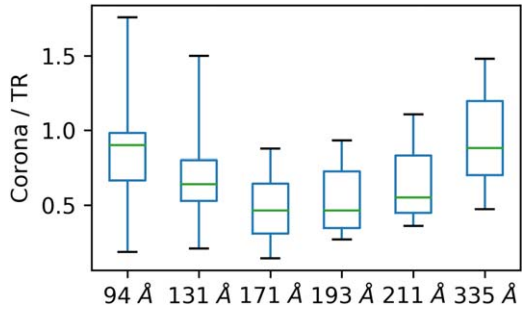

Figure 9. Observed $R_{C/TR}$ in the Warren et al. (2012) active regions. The green lines indicate the median of all the active regions, the box indicates the lower and upper quartiles, and the whiskers indicate the extremes. This plot is equivalent to the blue bars in Figure 7.

We can offer a partial explanation for the robust inverse correlation between α_{DEM} and $R_{C/TR}$ in the 131, 171, 193, and 211 Å channels. Consider, for example, the 211 Å channel with a peak response at 2 MK. This channel measures the corona of loops with coronal temperatures near 2 MK but the transition region of loops with coronal temperatures near 4 MK. Fundamentally, $R_{C/TR}$ in a given channel correlates positively with emission measure at the peak of the temperature response function and negatively with emission measure at temperatures greater than about twice the peak of the temperature response function. However, the exact explanation depends on the frequency with which the plasma is heated.

1. In the case of high-frequency heating, individual strands evolve very little. A shallow coronal DEM slope (small α_{DEM}) indicates that nearly as many strands are held at a quasi-constant coronal temperature of, say, 2 MK as are held at a quasi-constant coronal temperature of 4 MK. A steep slope (large α) indicates the dominance of hot strands. Consequently, $R_{C/TR}$ will be smaller (relatively brighter

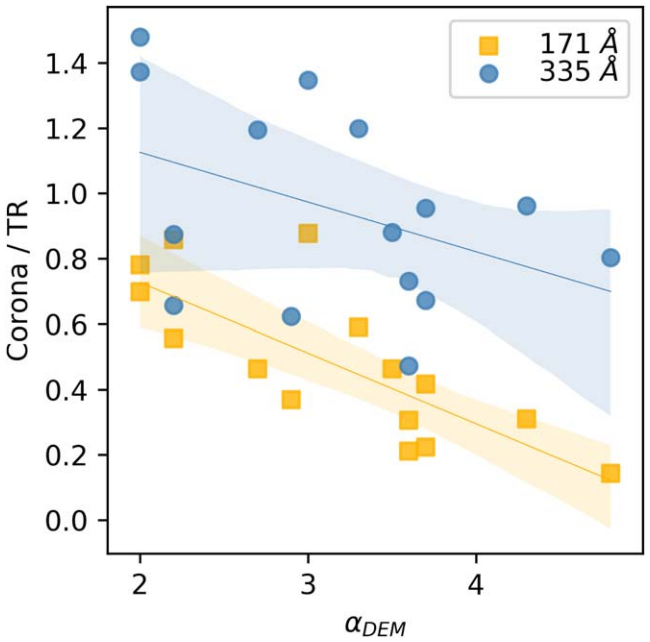

Figure 10. Correlation between $R_{C/TR}$ and α_{DEM} identified in Warren et al. (2012) for each active region in the 171 and 335 Å channels. The best-fit linear relationship and error region for each channel are plotted to guide the eye. Statistics about the relationship between $R_{C/TR}$ and α_{DEM} for each channel are given in Table 4.

Table 4
Correlation between α_{DEM} and $R_{C/TR}$

AIA Channel	r	$P(tw)$	χ	$\chi_{90\%}$
94 Å	−0.21	0.678	−0.10	−1.06 : 0.32
131 Å	−0.45	0.026	−0.74	−1.78 : −0.26
171 Å	−0.78	0.004	−1.78	−2.42 : −1.04
193 Å	−0.73	0.010	−1.12	−1.82 : −0.48
211 Å	−0.68	0.040	−0.80	−1.37 : −0.41
335 Å	−0.42	0.537	−0.50	−1.16 : 0.32

Note. r is the Pearson correlation coefficient between α_{DEM} and $R_{C/TR}$. $P(tw)$ is the probability of drawing the observed distribution from a uniform random distribution. χ is the most probable exponential in the relationship $R_{C/TR} \propto (\alpha_{DEM})^{\chi}$. $\chi_{90\%}$ is the 90% confidence interval of χ.

transition region) when the slope is steep (relatively more hot strands).

2. For low-frequency heating, the same argument as discussed in Section 2.4 applies. Strands experiencing low-frequency heating that begin their cooling from higher initial temperatures have smaller $R_{C/TR}$. Because α_{DEM} is calculated over a fixed temperature range ($6.0 \leqslant \log(T) \leqslant 6.6$), relatively more strands heated to peak temperatures coolward of $\log(T) = 6.6$ flatten the DEM (decreasing α_{DEM}) and result in larger $R_{C/TR}$.
3. In the intermediate frequency heating regime, strands cool partially before being reheated. A steep DEM slope (large α_{DEM}) indicates that relatively more strands begin their cooling at a higher maximum temperature and/or are reheated before cooling to lower temperatures. The same arguments that explain the anticorrelation between $R_{C/TR}$ and α_{DEM} in the low-frequency heating case apply here, with an additional, reinforcing effect. If the coronal segment of a strand never cools through the peak response of a given channel, that channel will collect even less coronal emission leading to a smaller $R_{C/TR}$.

These effects are not uniform across all AIA channels and depend on the shape of the temperature response function, but apply generally to the 131, 171, 193, and 211 Å channels that are quasi-isothermal with peak response below 2 MK. We also note that no model in Section 2 has exclusively high-, intermediate-, or low-frequency heating. They all include a mixture of the three, with the relative proportions being different from model to model. The same is likely true in these observed active regions.

4. Conclusion

Using the computational efficiency of EBTEL modeling and active regions studied by Warren et al. (2012) we investigated the theoretical and observed contribution of the transition region to AIA images. For this analysis, we defined the transition region from a physically meaningful perspective as the volume of the solar atmosphere above the chromosphere that is heated (while the corona is cooled) by thermal conduction, rather than more traditional observational definitions based on plasma temperature. With this definition, the transition region is confined to low altitudes, as in the conventional picture. This study involved two major investigations: an exploration of the parameter space of relevant coronal heating variables, with particular focus on the frequency of impulsive heating events, and a study of observed active regions to provide an observational anchor for the models.

The EBTEL models revealed that, consistent with previous studies (e.g., Patsourakos & Klimchuk 2008), imaging observations often described as "coronal" are expected to have significant contribution from transition region plasma. We find that the ratio of coronal to transition region emission is very different for the individual AIA channels and depends strongly on the heating parameters, demonstrating promising diagnostic potential. In general, we find that those scenarios with higher frequency heating events lead to higher time-averaged coronal temperatures and densities, but lower maximum temperatures and densities. However, observed intensities depend on the full DEM distribution, including both the coronal and transition region contributions, and it is not possible to easily predict the brightness in a channel based on the time-averaged coronal temperature and density alone. We also find that those strands subjected to the highest frequency heating agree quite well with theoretical expectations for coronal loops in static equilibrium. Overall, our analysis suggests that in shorter strands, the emission from the transition region and corona are comparable, while the emission from long strands tends to be dominated by the transition region, particularly in the higher frequency heating scenarios.

We performed a simple analysis of observed AIA active regions, comparing the intensity of emission from coronal and transition region plasma identified based on their morphology and relation to photospheric magnetic fields. Analyzing observations of active region NOAA 11268, we find an overall consistency with the models. The observations confirm the general trend in the models that the 335, 211 Å, and sometimes 94 Å channels (i.e., those associated with the hotter plasma) have the largest ratios and the 131, 171, and 193 Å channels

have the smallest ratios. The observed ratios depend, however, on assumptions about how much overlying coronal emission is present above the footpoint transition region emission. These same observational trends persist when analyzing the 15 active regions from Warren et al. (2012), although they have generally higher ratios. All of these active regions suggest that AIA observations of loops sample a similar level of emission from the corona and transition region.

We also analyzed the relationships between $R_{C/TR}$ and the slopes of the DEMs determined by Warren et al. (2012). We find that there is a consistent negative relationship between the slope of the DEM coolward of the temperature peak and $R_{C/TR}$ in the observed regions. This is consistent with theoretical expectations based on low, intermediate, or high frequency impulsive heating.

We note that, particularly for the longer 80 Mm strands, the models suggest that the ratio of coronal to transition region intensity should be significantly smaller than is observed. One potential explanation for this is the absorption of transition region emission from spicules extending from the underlying chromosphere. This has been found to cause up to a factor of 2 decrease in the observed transition region intensity (De Pontieu et al. 2009), which would increase the observed ratios compared to model predictions, consistent with our findings.

We made no attempt to ascribe a particular heating model to the studied active regions because individual zero-dimensional EBTEL models are inadequate to properly characterize the complexity of active region observations. It is unreasonable to expect the model of a single magnetic strand to replicate observations from even simple active regions. In addition, there is ambiguity due to the somewhat arbitrary choice of observational path length assigned to the coronal emission in the EBTEL models. Both of these uncertainties can be largely resolved by studying this effect in three-dimensional models of active regions where the true extent of the corona can be more accurately estimated. We have begun to construct such models, based on observed photospheric magnetograms, using the approach described in Nita et al. (2018).

Despite the idealized nature of the modeling and observational analyses presented here, they clearly demonstrate the importance of considering the transition region in active region models, particularly when they are used to study coronal heating. Depending on how the active region is heated, failing to include the transition region could lead to significant underestimation of the AIA emission from the region.

Data supplied courtesy of the SDO/HMI and SDO/AIA consortia. SDO is the first mission launched for NASA's Living With a Star (LWS) Program. EBTEL++ is developed and maintained by the Rice University Solar Physics Research Group. S.J.S.'s research was supported by an appointment to the NASA Postdoctoral Program at the Goddard Space Flight Center, administered by Universities Space Research Association under contract with NASA. This work of J.A.K. was supported by the Goddard Space Flight Center Internal Scientist Funding Model (competitive work package) program.

ORCID iDs

S. J. Schonfeld https://orcid.org/0000-0002-5476-2794
J. A. Klimchuk https://orcid.org/0000-0003-2255-0305

References

Barnes, W. T., Bradshaw, S. J., & Viall, N. M. 2019, ApJ, 880, 56
Barnes, W. T., Cargill, P. J., & Bradshaw, S. J. 2016a, ApJ, 829, 31
Barnes, W. T., Cargill, P. J., & Bradshaw, S. J. 2016b, ApJ, 833, 217
Bradshaw, S. J., & Cargill, P. J. 2013, ApJ, 770, 12
Bradshaw, S. J., Del Zanna, G., & Mason, H. E. 2004, A&A, 425, 287
Bradshaw, S. J., & Klimchuk, J. A. 2011, ApJS, 194, 26
Bradshaw, S. J., & Mason, H. E. 2003a, A&A, 401, 699
Bradshaw, S. J., & Mason, H. E. 2003b, A&A, 407, 1127
Bradshaw, S. J., & Viall, N. M. 2016, ApJ, 821, 63
Cargill, P. J. 1994, ApJ, 422, 381
Cargill, P. J. 2014, ApJ, 784, 49
Cargill, P. J., Bradshaw, S. J., & Klimchuk, J. A. 2012a, ApJ, 752, 161
Cargill, P. J., Bradshaw, S. J., & Klimchuk, J. A. 2012b, ApJ, 758, 5
Cargill, P. J., & Klimchuk, J. a. 2004, ApJ, 605, 911
Cranmer, S. R., & Winebarger, A. R. 2019, ARA&A, 57, 157
De Pontieu, B., Hansteen, V. H., McIntosh, S. W., & Patsourakos, S. 2009, ApJ, 702, 1016
Dere, K. P., Landi, E., Mason, H. E., Monsignori Fossi, B. C., & Young, P. R. 1997, A&AS, 125, 149
Efron, B., & Petrosian, V. 1992, ApJ, 399, 345
Guarrasi, M., Reale, F., Orlando, S., Mignone, A., & Klimchuk, J. A. 2014, A&A, 564, A48
Handy, B. N., Acton, L. W., Kankelborg, C. C., et al. 1999, SoPh, 187, 229
Hinode Review Team, Al-Janabi, K., Antolin, P., et al. 2019, PASJ, 71, R1
Johnston, C. D., Cargill, P. J., Antolin, P., et al. 2019, A&A, 625, A149
Johnston, C. D., Hood, A. W., Cargill, P. J., & De Moortel, I. 2017a, A&A, 597, A81
Johnston, C. D., Hood, A. W., Cargill, P. J., & De Moortel, I. 2017b, A&A, 605, A8
Klimchuk, J. A. 2006, SoPh, 234, 41
Klimchuk, J. A. 2015, RSPTA, 373, 20140256
Klimchuk, J. A., & Bradshaw, S. J. 2014, ApJ, 791, 60
Klimchuk, J. A., Patsourakos, S., & Cargill, P. J. 2008, ApJ, 682, 1351
Knizhnik, K. J., & Reep, J. W. 2020, SoPh, 295, 21
Knizhnik, K. J., Uritsky, V. M., Klimchuk, J. A., & DeVore, C. R. 2018, ApJ, 853, 82
Landi, E., Young, P. R., Dere, K. P., Del Zanna, G., & Mason, H. E. 2013, ApJ, 763, 86
Lemen, J. R., Boerner, P. F., Edwards, C. G., et al. 2012, SoPh, 275, 17
Lionello, R., Alexander, C. E., Winebarger, A. R., Linker, J. A., & Mikić, Z. 2016, ApJ, 818, 129
López Fuentes, M., & Klimchuk, J. A. 2015, ApJ, 799, 128
Lundquist, L. L., Fisher, G. H., & Mctiernan, J. M. 2008a, ApJS, 179, 509
Lundquist, L. L., Fisher, G. H., Metcalf, T. R., Leka, K. D., & Mctiernan, J. M. 2008b, ApJ, 689, 1388
Mandrini, C. H., Démoulin, P., & Klimchuk, J. A. 2000, ApJ, 530, 999
Marsh, A. J., Smith, D. M., Glesener, L., et al. 2018, ApJ, 864, 5
Nita, G. M., Viall, N. M., Klimchuk, J. A., et al. 2018, ApJ, 853, 66
Parker, E. N. 1988, ApJ, 330, 474
Parnell, C. E., & De Moortel, I. 2012, RSPTA, 370, 3217
Patsourakos, S., & Klimchuk, J. A. 2008, ApJ, 689, 1406
Pesnell, W. D., Thompson, B. J., & Chamberlin, P. C. 2011, SoPh, 275, 3
Porter, L. J., & Klimchuk, J. A. 1995, ApJ, 454, 499
Reep, J. W., Bradshaw, S. J., & Klimchuk, J. A. 2013, ApJ, 764, 193
Rosner, R., Tucker, W. H., & Vaiana, G. S. 1978, ApJ, 220, 643
van den Oord, G. H. J. 1994, in IAU Coll. 144 Solar Coronal Structures, ed. V. Rusin, P. Heinzel, & J.-C. Vial (Tatranska Lomnica: Veda Publishing Company), 11
Vesecky, J. F., Antiochos, S. K., & Underwood, J. H. 1979, ApJ, 233, 987
Viall, N. M., De Moortel, I., Downs, C., et al. 2020, Earth and Space Science Open Archive, 94, doi:10.1002/essoar.10502697.1
Viall, N. M., & Klimchuk, J. A. 2011, ApJ, 738, 24
Viall, N. M., & Klimchuk, J. A. 2013, ApJ, 771, 115
Viall, N. M., & Klimchuk, J. A. 2017, ApJ, 842, 108
Walsh, R. W., & Ireland, J. 2003, A&ARv, 12, 1
Warren, H. P., Kim, D. M., DeGiorgi, A. M., & Ugarte-Urra, I. 2010, ApJ, 713, 1095
Warren, H. P., & Winebarger, A. R. 2006, ApJ, 645, 711
Warren, H. P., & Winebarger, A. R. 2007, ApJ, 666, 1245
Warren, H. P., Winebarger, A. R., & Brooks, D. H. 2012, ApJ, 759, 141
Warren, H. P., Winebarger, A. R., & Hamilton, P. S. 2002, ApJL, 579, L41
Withbroe, G. L., & Noyes, R. W. 1977, ARA&A, 15, 363
Zirker, J. B. 1993, SoPh, 148, 43